Gravity-driven granular free-surface flow around a circular cylinder

X. Cui[1],[†] and J. M. N. T. Gray[2]

[1]Aerospace Engineering, Department of Engineering and Mathematics, Sheffield Hallam University, Sheffield S1 1WB, UK

[2]School of Mathematics and Manchester Centre for Nonlinear Dynamics, University of Manchester, Manchester M13 9PL, UK

Snow avalanches and other hazardous geophysical granular flows, such as debris flows, lahars and pyroclastic flows, often impact on obstacles as they flow down a slope, generating rapid changes in the flow height and velocity in their vicinity. It is important to understand how a granular material flows around such obstacles to improve the design of deflecting and catching dams, and to correctly interpret field observations. In this paper small-scale experiments and numerical simulations are used to investigate the supercritical gravity-driven free-surface flow of a granular avalanche around a circular cylinder. Our experiments show that a very sharp bow shock wave and a stagnation point are generated in front of the cylinder. The shock standoff distance is accurately reproduced by shock-capturing numerical simulations and is approximately equal to the reciprocal of the Froude number, consistent with previous approximate results for shallow-water flows. As the grains move around the cylinder the flow expands and the pressure gradients rapidly accelerate the particles up to supercritical speeds again. The internal pressure is not strong enough to immediately push the grains into the space behind the cylinder and instead a grain-free region, or granular vacuum, forms on the lee side. For moderate upstream Froude numbers and slope inclinations, the granular vacuum closes up rapidly to form a triangular region, but on steeper slopes both experiments and numerical simulations show that the pinch-off distance moves far downstream.

Key words: compressible flows, granular media, shock waves

1. Introduction

Gravity-driven granular free-surface flows, or granular avalanches, are more common than one might imagine. They occur whenever grains are poured (Boudet *et al.* 2007; Johnson & Gray 2011), flow in chutes (Savage 1979; Akers & Bokhove 2008) or are rotated in drums and industrial mixers (Shinbrot & Muzzio 1998; Gray 2001). Hazardous geophysical mass flows, such as snow avalanches (Savage & Hutter 1989; Jóhannesson 2001; Jomelli & Bertran 2001), debris flows (Iverson & Denlinger 2001;

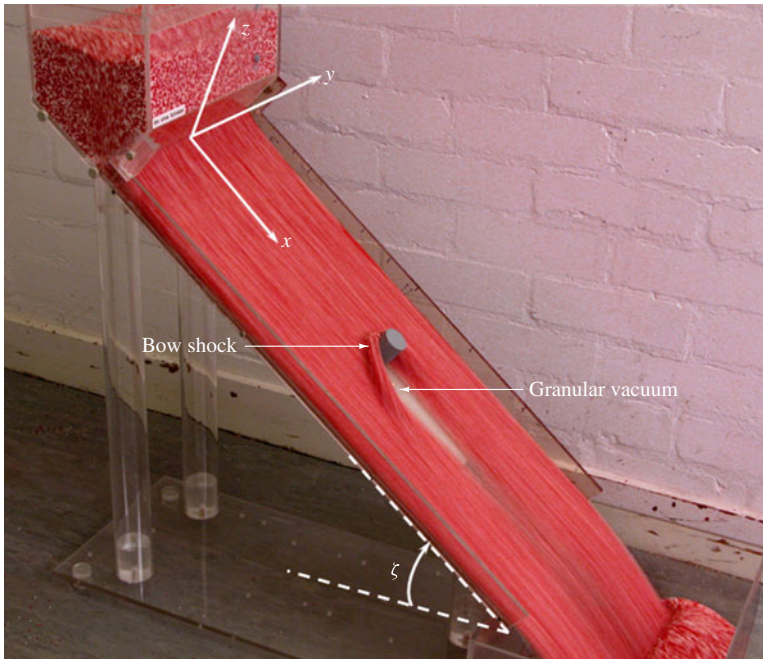† Email address for correspondence: x.cui@shu.ac.uk

FIGURE 1. Experimental set-up showing the flow of non-pareille grains (commonly known as 100s and 1000s or sprinkles) past a circular cylinder on a chute inclined at an angle ζ to the horizontal. The x-coordinate is aligned with the downslope direction, the y-coordinate is across the chute and z is the upward pointing normal.

Johnson *et al.* 2012), lahars (Vallance 2000) and pyroclastic flows (Branney & Kokelaar 1992; Cole *et al.* 1998; Mangeney *et al.* 2007) are all forms of granular free-surface flows that occur regularly in our natural environment. Despite the enormous difference in scales these examples are all commonly modelled using depth-averaged shallow-water type theories that have additional momentum source terms (Grigourian, Eglit & Iakimov 1967; Savage & Hutter 1989; Iverson 1997; Gray, Wieland & Hutter 1999; Gray, Tai & Noelle 2003; Mangeney-Castelnau *et al.* 2003). These relatively simple theories have proved to be particularly effective at modelling geophysical flows as well as being able to accurately reproduce carefully controlled small-scale experiments.

The study of granular flows past obstacles, see for example figure 1, has attracted much attention in recent years, because of its importance in the design of deflecting and catching dams (Sigurdsson, Tomasson & Sandersen 1998; Tai *et al.* 1999; Cui, Gray & Johannesson 2007; Hauksson *et al.* 2007; Jóhannesson *et al.* 2009). These are used extensively in mountainous regions to protect people and infrastructure from geophysical mass flows. As well as being able to fly over, or overtop, these defensive structures (Hákonardóttir *et al.* 2003; Faug *et al.* 2008) they also generate shock waves in front of, or adjacent to, them, at which there are rapid changes in the avalanche thickness and flow velocity (e.g. Tai *et al.* 2001; Gray *et al.* 2003). Shock waves arise naturally from the hyperbolic structure of the shallow-water equations. In two dimensions there are stationary granular jumps, that are analogous to hydraulic jumps in open channel flows (Savage 1979; Brennen, Sieck & Paslaski 1983), as well as propagating granular bores that bring material rapidly to rest (Gray & Hutter 1997;

Gray & Tai 1998). In three dimensions, weak, strong and detached oblique shocks develop when the oncoming flow is deflected by a sharp tipped wedge (Gray *et al.* 2003; Hákonardóttir & Hogg 2005; Cui *et al.* 2007; Gray & Cui 2007; Vreman *et al.* 2007; Akers & Bokhove 2008), which are analogous to oblique shocks in shallow water (Preiswerk 1938; Rouse 1938; Ippen 1949) and gas dynamic flows (Ames Research Staff 1953). Unsteady inward-propagating granular jumps form when a jet of grains hits a flat plate (Boudet *et al.* 2007) and when the plate is inclined, a rich variety of steady and unsteady shock waves form (Johnson & Gray 2011). In dilute granular flows, shock waves in density and velocity develop instead, and highly agitated low solids volume fraction flows past wedges (Rericha *et al.* 2002) and cylinders (Buchholtz & Pöschel 1998; Wassgren *et al.* 2003; Boudet & Kellay 2010) have also been investigated in this context. High-speed dilute and dense granular flows exhibit similar shock waves to those observed in gas dynamics and shallow water flow; which themselves have a well-known relationship between them (Preiswerk 1938; Courant & Friedrichs 1948).

The aim of this paper is to investigate what happens when a dense granular avalanche impacts on a blunt body, described by a wall boundary, rather than a sharp tipped wedge (e.g. Gray & Cui 2007) or a topographic feature with a finite slope, such as a pyramidal obstacle (Gray *et al.* 2003). It is shown how a body-fitted grid (Vinokur 1974; Viviand 1974) combined with shock-capturing numerical methods (e.g. Godunov 1959; Nessyahu & Tadmor 1990; LeVeque 2002) can be used to solve for the motion around an arbitrarily shaped walled obstacle. The particular case that we focus on is that of a circular cylinder, which is not only a classical shape, but is of fundamental practical interest for the design of pylons that are able to withstand such flows (Sovilla *et al.* 2008), as well as being representative of common obstacles such as tree trunks. To provide basic physical insight into the problem as well as quantitative data to compare the model against, we begin by performing a series of small-scale experiments.

2. Small-scale experiments

The experimental set-up is shown in figure 1. It consists of a smooth Plexiglas chute that is 300 mm wide and 600 mm long and is inclined at an angle ζ to the horizontal. At the top of the chute is a hopper, where the grains are loaded, and there is a gate mechanism that controls the height and flux of material entering the chute. A 30 mm diameter circular metal cylinder is attached in the centre of the chute 300 mm downstream of the inflow gate, so that its axis of revolution is normal to the inclined plane. The flow in figure 1 shows a thin, rapidly moving, avalanche of non-pareille (commonly known as hundreds and thousands or sprinkles) on a slope inclined at $\zeta = 38°$. The grains are approximately 1 mm in diameter and are coloured red and white. Individual grains can be identified in the hopper where there is relatively little motion adjacent to most of the transparent sidewalls. A relatively long exposure is used to produce surface streaks and help visualize the particle trajectories. Just upstream of the cylinder there is a strong jump in the flow thickness and velocity, which is termed a 'bow shock wave'. On the lee side a particle-free region forms, which is termed a 'granular vacuum' by direct analogy with vacuum boundaries in gas dynamics, where the density, ρ, is zero, rather than the avalanche thickness, h. Grains run freely off the end of the chute into a collecting box, so there is no significant upstream influence by the outflow conditions.
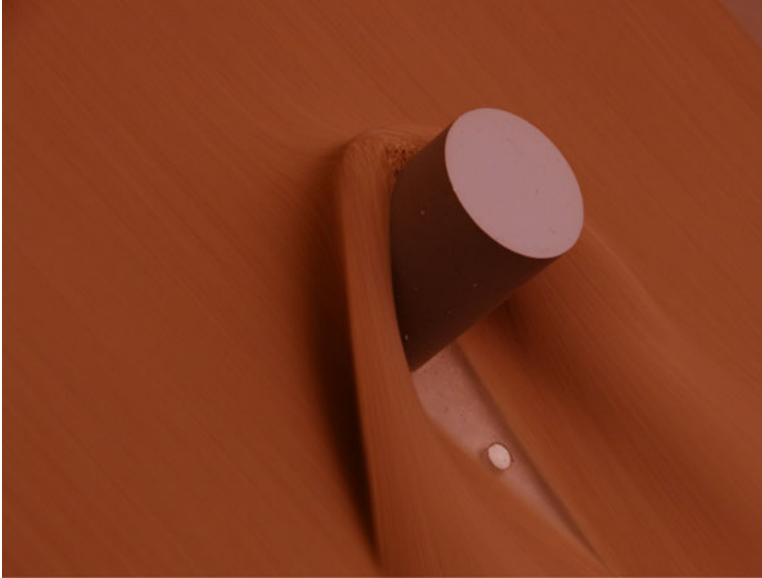
FIGURE 2. Perspective view of a bow shock, stagnation point and particle-free granular vacuum, generated when a sand avalanche flows around a circular cylinder. The chute is inclined at $\zeta = 36°$ to the horizontal and the Froude number just upstream of the shock is approximately equal to six. The flow is from top left to bottom right. Individual grains can be seen near the stagnation point.

The formation of shock waves is insensitive to the particular type of granular material used, although the resolution of the shocks is better if the grains are small relative to the typical scale of flow features. Figures 2 and 3 show closeup oblique and overhead views of the steady fully developed flow of a soft masonry sand avalanche around the circular cylinder on a $\zeta = 36°$ slope. The sand is polydisperse, but the majority of grains lie in the range 100–400 μm and although they are not of contrasting colour, they still produced subtle streak lines in the photographs that reveal the particle paths. The bow shock starts just upstream of the obstacle and is very abrupt, appearing as a sharp line in the overhead view in figure 3, which wraps around on either side of the cylinder. It separates the oncoming supercritical flow (where the Froude number $Fr > 1$) from the deflected flow on the downstream side, which has regions of both subcritical ($Fr < 1$) and supercritical flow. The deflected flow appears slightly lighter than the oncoming flow, in figure 3, due to the lighting. The avalanche thickens significantly across the shock, rising to a maximum height immediately above the furthest upstream point on the cylinder wall. This is also where the stagnation point is located. The flow is slowed so much near the stagnation point that it is possible to just see some of the individual particles in the photographs in figures 2 and 3.

As the grains move around the top side of the cylinder the flow expands, causing the thickness to decrease and the grains to rapidly accelerate reaching supercritical speeds again. The dividing line between subcritical and supercritical flow is called the 'critical line' and is where $Fr = 1$. Close to the wall the avalanche develops steep sides that cast a shadow on either side of the cylinder as shown in figure 3. This part of the expansion is so strong that the avalanche reaches zero thickness before the two streams meet and the flow detaches from the wall. Downstream the grains are pushed inwards
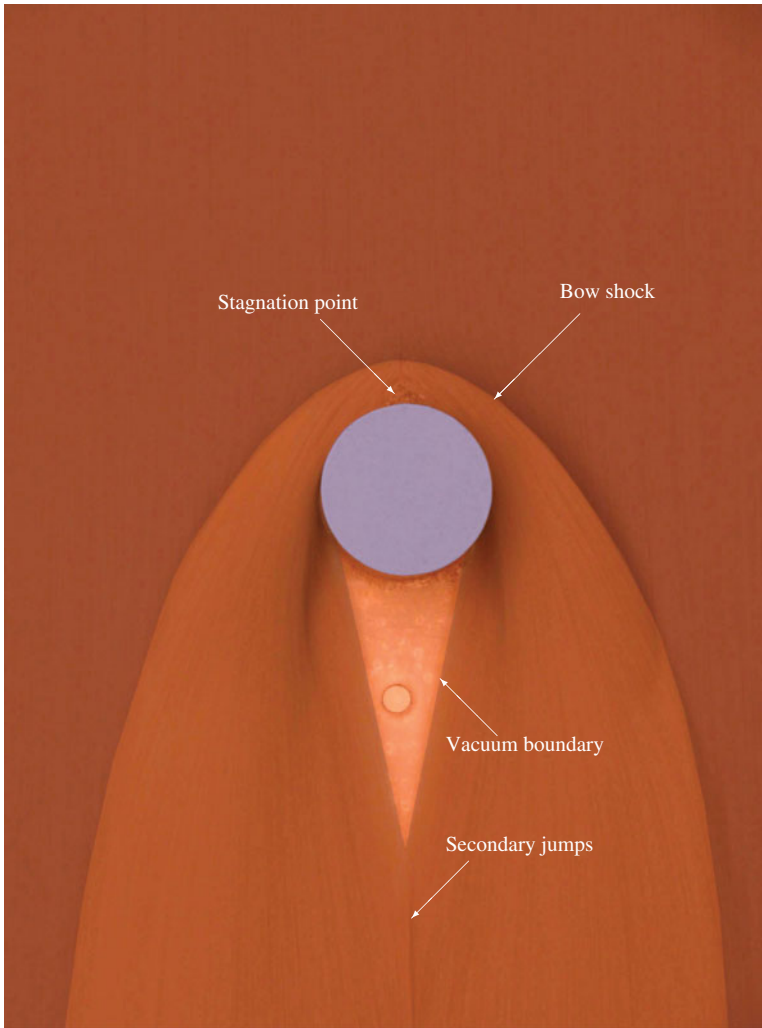
FIGURE 3. Overhead view of the bow shock, stagnation point and particle free-granular vacuum, under the same conditions as in figure 2. The flow is from top to bottom. Individual sand grains can be seen near the stagnation point.

on either side by the lateral pressure gradients, and the zero thickness boundary moves inwards and eventually intersects at a sharp point some distance downstream. The sides of this grain-free region are almost straight, so the granular vacuum on the lee side looks triangular in shape. The point of intersection of the two streams, or pinch-off point, is similar to those observed by Johnson & Gray (2011) during jet impingement on a plane. In this case, however, there is no flux of grains from the vacuum region.

3. Governing equations

We use the dimensionless model formulated by Gray *et al.* (2003) in our discussion. It is set up in a coordinate system, *Oxyz*, with the *x*-axis pointing down a plane inclined at ζ to the horizontal, the *y*-axis pointing across the slope and *z*-axis being

the upward pointing normal, as shown in figure 1. The depth-integrated mass and momentum balance equations are

$$\frac{\partial h}{\partial t} + \frac{\partial}{\partial x}(h\bar{u}) + \frac{\partial}{\partial y}(h\bar{v}) = 0, \tag{3.1}$$

$$\frac{\partial}{\partial t}(h\bar{u}) + \frac{\partial}{\partial x}(\lambda h\bar{u}^2) + \frac{\partial}{\partial y}(\lambda h\bar{u}\bar{v}) + \frac{\partial}{\partial x}\left(\frac{1}{2}h^2\cos\zeta\right) = hS_1, \tag{3.2}$$

$$\frac{\partial}{\partial t}(h\bar{v}) + \frac{\partial}{\partial x}(\lambda h\bar{u}\bar{v}) + \frac{\partial}{\partial y}(\lambda h\bar{v}^2) + \frac{\partial}{\partial y}\left(\frac{1}{2}h^2\cos\zeta\right) = hS_2, \tag{3.3}$$

respectively. The avalanche thickness, h, and the depth-averaged velocity, $\bar{\boldsymbol{u}} = (\bar{u}, \bar{v})$, in the downslope and cross-slope directions have been non-dimensionalized using the scalings

$$\tilde{h} = Lh, \quad (\tilde{x}, \tilde{y}) = L(x, y), \quad (\tilde{\bar{u}}, \tilde{\bar{v}}) = \sqrt{Lg}\,(\bar{u}, \bar{v}), \quad \tilde{t} = \sqrt{(L/g)}\,t, \tag{3.4}$$

where the tildered variables are dimensional, g is the constant of gravitational acceleration and L is the diameter of the cylinder. For the experiments in this paper, $L = 0.03$ m, which implies that the velocities are scaled by $\sqrt{Lg} = 0.54$ m s^{-1} and time is scaled by $\sqrt{L/g} = 0.055$ s. The source terms S_1 and S_2 on the right-hand side of (3.2) and (3.3) are composed of the downslope component of gravity, which drives the avalanche downslope, and Coulomb basal friction, which resists the motion

$$S_1 = \sin\zeta - \mu(\bar{u}/|\bar{\boldsymbol{u}}|)\cos\zeta, \tag{3.5}$$
$$S_2 = -\mu(\bar{v}/|\bar{\boldsymbol{u}}|)\cos\zeta, \tag{3.6}$$

where $\mu = \tan\delta$ is the coefficient of friction and δ is the dynamic basal angle of friction. The parameter λ arises during depth integration of the momentum transport terms, since the average of the product of two velocity components is not equal to the product of the average of those velocity components. Usually these factors are assumed to be unity, which is equivalent to the assumption that velocity profiles are uniform with depth. Assuming that the lateral and downslope velocity profiles, (u, v), are of the same form, the parameter λ is the same for each product, and is defined as

$$\lambda = \frac{1}{h\bar{u}^2}\int_0^h u^2\,\mathrm{d}z = \frac{1}{h\bar{u}\bar{v}}\int_0^h uv\,\mathrm{d}z = \frac{1}{h\bar{v}^2}\int_0^h v^2\,\mathrm{d}z. \tag{3.7}$$

Various authors have considered the effect of other assumed profiles. Savage & Hutter (1989) showed that $\lambda = 6/5$ for a parabolic velocity profile, Pouliquen & Forterre (2002) obtained the value of 4/3 for a linear profile (with no basal slip), and Börzsönyi, Halsey & Ecke (2008) showed that for a convex Bagnold profile, $\lambda = 5/4$. On rough beds Pouliquen & Forterre (2002) showed that numerical computations are relatively insensitive to the value of λ because the flows are sufficiently slow that the momentum transport terms do not play a large role. Nevertheless, deviations of λ away from unity can cause difficulties near vacuum boundaries, since the characteristic surface no longer coincides with the motion of the boundary and the degenerate nature of the equations is lost. Such problems are often circumvented by requiring the shape factor $\lambda \longrightarrow 1$ as $h \longrightarrow 0$.

In this paper, the flows are strongly accelerated, which implies that the momentum transport terms play a much more important role than for slow flows on rough beds. However, there is also a greater degree of basal slip. The lateral velocities may

reasonably be approximated by the linear profiles

$$u = \bar{u}\left(\alpha + 2(1-\alpha)\frac{z}{h}\right), \quad v = \bar{v}\left(\alpha + 2(1-\alpha)\frac{z}{h}\right), \tag{3.8}$$

which give plug flow ($\alpha = 1$), simple shear ($\alpha = 0$) and linear shear with basal slip for $\alpha \in (0, 1)$. For these profiles the parameter

$$\lambda = \tfrac{1}{3}(4 - 2\alpha + \alpha^2). \tag{3.9}$$

For a typical value of $\alpha = 0.75$, the shape factor $\lambda = 1.0208$, which is sufficiently close to unity that we shall assume $\lambda = 1$. In this case the Froude number

$$Fr = |\bar{\boldsymbol{u}}|/c, \tag{3.10}$$

is defined as the ratio of the flow speed $|\bar{\boldsymbol{u}}|$ to the wavespeed $c = \sqrt{h \cos \zeta}$. The major difference of the avalanche equations (3.1)–(3.3) to standard shallow-water flows is the presence of the source terms on the right-hand side.

4. Steady state accelerating flows on a smooth bed

In the chute flow experiments, shown in figures 1–3, the base is relatively smooth and the grains are able to accelerate downslope rather than attaining a steady uniform velocity, as they might on a rough bed (Pouliquen 1999; Pouliquen & Forterre 2002). This leads to a considerable thinning of the flow as it exits the gate as shown in figure 4. The acceleration is controlled by the dynamic angle of friction δ, which characterizes the rate-independent Coulomb friction that is generated at the base by the slightly dilated agitated flow of grains above. It is usually several degrees less than the microscopic static basal friction angle. In this section a new method for determining δ is described, which is based on constructing a one-dimensional exact solutions for the accelerating flow. Assuming that the flow is steady, and $\bar{v}$ is identically zero, the mass balance equation (3.1) and the downslope momentum balance equation (3.2) reduce to

$$\frac{\partial}{\partial x}(h\bar{u}) = 0, \tag{4.1}$$

$$\frac{\partial}{\partial x}\left(h\bar{u}^2 + \frac{1}{2}h^2 \cos \zeta\right) = hS_1, \tag{4.2}$$

where the source term S_1 is now constant, i.e.

$$S_1 = \sin \zeta - \tan \delta \cos \zeta = \sec \delta \sin \beta, \tag{4.3}$$

and the angle

$$\beta = \zeta - \delta, \tag{4.4}$$

is the difference between the slope inclination and the basal angle of friction. The mass balance equation (4.1) can be integrated directly, subject to the boundary condition that the avalanche velocity and thickness at the inflow are $\bar{u}_0$ and h_0, respectively, to give a relation between the flow thickness and the velocity

$$h\bar{u} = h_0 \bar{u}_0. \tag{4.5}$$

The momentum balance equation (4.2) can be simplified by expanding out the derivatives, using (4.1) and then dividing through by h to give

$$\bar{u}\frac{\partial \bar{u}}{\partial x} + \cos \zeta \frac{\partial h}{\partial x} = S_1. \tag{4.6}$$
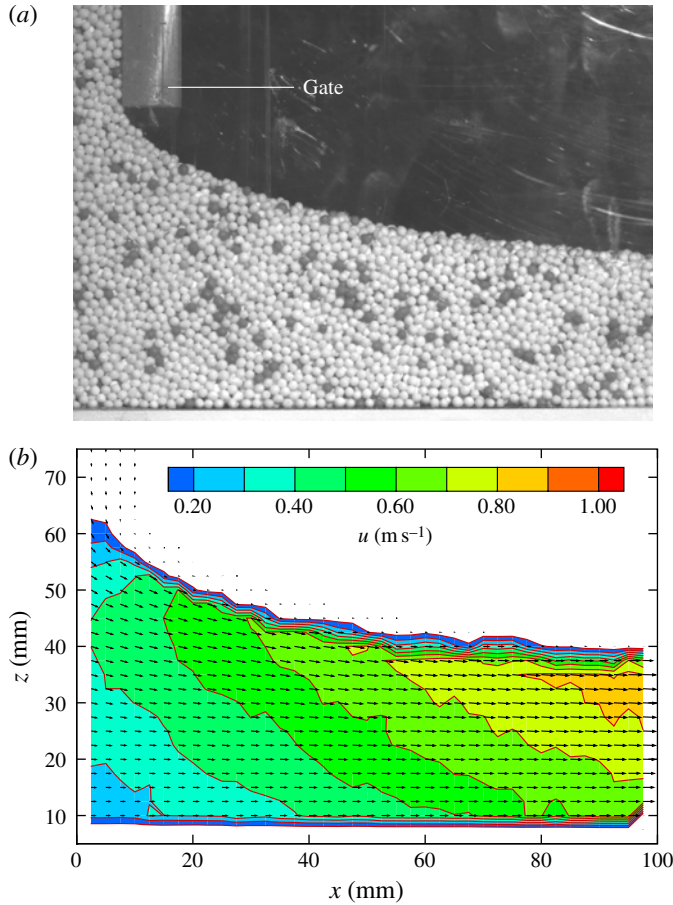
(*a*)

(*b*)

FIGURE 4. (*a*) A photograph through the transparent sidewall of the chute showing how an avalanche of non-pareille exits under a control gate at a Froude number of approximately $Fr = 1.42$ and dramatically thins as it accelerates downslope. The camera and the chute are both inclined at an angle of $38°$ to the horizontal. (*b*) A PIV measurement of the velocity vectors overlapped with the contour lines of the downslope velocity u in metres per second.

Using (4.5) to substitute for the avalanche thickness, (4.6) can be integrated, subject to the condition that the inflow lies at $x = 0$, to give a cubic equation for the avalanche velocity

$$\bar{u}^3 - (2S_1 x + \bar{u}_0^2 + 2h_0 \cos \zeta)\bar{u} + 2h_0 \bar{u}_0 \cos \zeta = 0. \tag{4.7}$$

This can either be solved by numerical root finding techniques or by using Cardano's formula for $\bar{u} = \bar{u}(x)$. For inflow Froude numbers above unity there are three real solutions for $x > 0$. One is strictly negative, the other two are positive, by Descartes' rule of signs, and correspond to an accelerating and a decelerating flow, respectively. The decelerating solution can be physically realized by using downstream control gates (see, e.g., Gray & Cui 2007), but normally the accelerating solution is selected. This necessarily has a decreasing thickness distribution, which can be calculated from (4.5).

The solution provides two very simple ways of determining the dynamic basal angle of friction, δ. One strategy is to measure the thickness of the flow as a
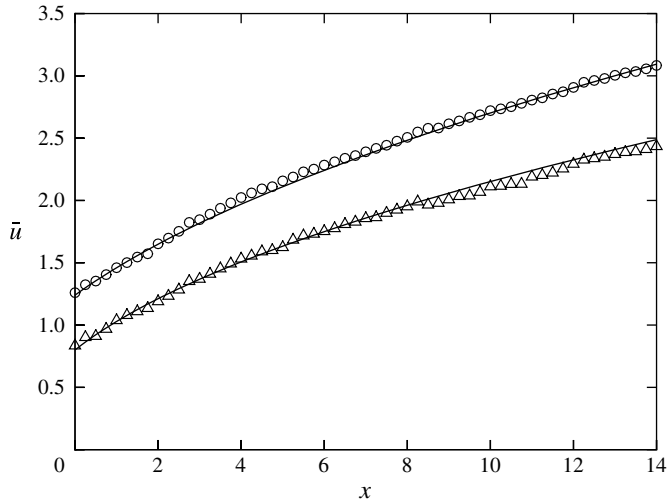
FIGURE 5. A comparison between the exact solution (solid lines) for $\bar{u}(x)$ and surface PIV measurements for non-pareille (circles) and sand (triangles). The experiment with non-pareille was performed on a chute inclined at $\zeta = 38°$ and an inflow gate height $h_0 = 0.43$. The best fit was obtained with an inflow velocity $\bar{u}_0 = 1.24$ and basal angle of friction $\delta = 23°$. The sand experiments were performed with an inflow height of $h_0 = 0.4$ and a slope of $\zeta = 36°$ and the best fit was found with $\delta = 26°$ for $\bar{u}_0 = 0.8$.

function of x and the steady-state mass flux, m_{exit}, per unit width at the end of the chute. For an inflow gate height, h_0, the depth-averaged velocity at the inflow is $\bar{u}_0 = m_{exit}/h_0$, provided (4.1) holds. The value of δ can then be determined by fitting the exact solution to the measured thickness h. This approach relies on being able to measure small height variations very accurately. Alternatively, particle image velocimetry (PIV) can be used to measure the surface velocity as a function of x. Figure 5 shows two sets of surface velocity measurements for non-pareille (also known as 100s and 1000s or sprinkles) and for sand. This has the advantage that the surface velocity is considerably easier to measure and has larger variation than the thickness. However, this is not the depth-averaged velocity, $\bar{u}$, and an assumption about the downslope velocity profile with depth (3.8) needs to be made to relate the two. Figure 4(b) shows PIV measurements through the sidewall of the chute for a relatively thick flow exiting the hopper. While these velocities may be effected by the sidewall friction they indicate that the velocity profile is plug-like with only a relatively small amount of vertical shear. For simplicity, we shall therefore assume plug flow, i.e. the surface velocity is equal to the depth-averaged velocity, which may lead to a small overestimate of the depth-averaged velocity. Setting the inflow velocity, $\bar{u}_0$, and then matching the solution $\bar{u}(x)$ to the data yields the dynamic basal angle of friction. For non-pareille $\delta = 23°$. While for fine sand $\delta = 26°$. This approach is a considerable improvement on previous measurement techniques for δ (Hungr & Morgenstern 1984a,b; Savage & Hutter 1989; Wieland, Gray & Hutter 1999). Furthermore, the two methods can also be used in combination to constrain the solution even further. For instance, it may yield useful information on the degree of shear through the layer or changes in bulk density.
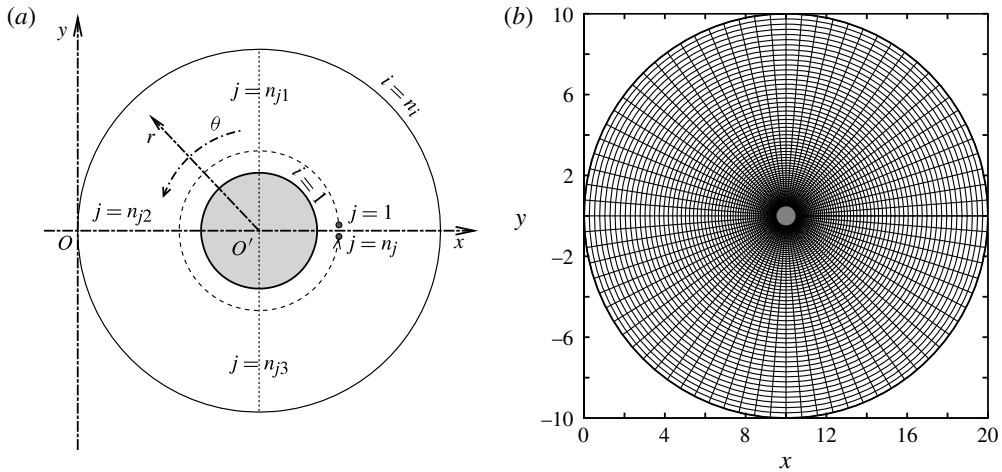
FIGURE 6. Coordinate mapping (*a*) between rectangular *Oxy* and polar *O′rθ* coordinates, with the origin *O* at the hopper gate and *O′* centred on the cylindrical obstacle. An *O*-type grid (*b*) is used in the computation, where *i* denotes the radial coordinate from 1 (cylinder wall) to n_i (outer boundary) and *j* denotes the circumferential grid points anti-clockwise from 1 to n_j.

5. Numerical method

The boundary conditions on the wall of the cylinder are more easily applied by solving the governing equations in a body fitted coordinate system. This transformation is achieved by using the conservative variables h, $m = h\bar{u}$ and $n = h\bar{v}$ to write the system of equations (3.1)–(3.3) in vector form as

$$\frac{\partial \boldsymbol{U}}{\partial t} + \frac{\partial \boldsymbol{E}}{\partial x} + \frac{\partial \boldsymbol{F}}{\partial y} = \boldsymbol{S}, \tag{5.1}$$

where $\boldsymbol{U} = (h, m, n)^{\mathrm{T}}$ is the vector of conservative variables and the superscript T denotes the matrix transpose. The respective flux and source term vectors are

$$\boldsymbol{E} = (m, m^2/h + h^2 \cos \zeta /2, mn/h)^{\mathrm{T}}, \tag{5.2a}$$

$$\boldsymbol{F} = (n, mn/h, n^2/h + h^2 \cos \zeta /2)^{\mathrm{T}}, \tag{5.2b}$$

$$\boldsymbol{S} = (0, hS_1, hS_2)^{\mathrm{T}}. \tag{5.2c}$$

For computing the flow around a circular cylinder the body fitted coordinates reduce to a polar coordinate system $O′r\theta$ defined by

$$r = \sqrt{(x - 10)^2 + y^2}, \quad \theta = \tan^{-1}\left(\frac{y}{x - 10}\right), \quad \tau = t, \tag{5.3}$$

as shown in figure 6. Note that the origin $O′$ is centred on the cylinder and there is therefore an offset of 10 non-dimensional units (30 cm) from the outflow gate at $x = 0$. The transformed equations are not in conservative form, but they can be written in conservative form (see, e.g., Vinokur 1974; Viviand 1974; Anderson 1995, pp. 183–186)

$$\frac{\partial \hat{\boldsymbol{U}}}{\partial \tau} + \frac{\partial \hat{\boldsymbol{E}}}{\partial r} + \frac{\partial \hat{\boldsymbol{F}}}{\partial \theta} = \hat{\boldsymbol{S}}, \tag{5.4}$$

by defining the new conservative variables, fluxes and the source terms as

$$\hat{U} = J^{-1}U, \quad \hat{E} = J^{-1}(r_x E + r_y F), \quad \hat{F} = J^{-1}(\theta_x E + \theta_y F), \quad \hat{S} = J^{-1}S, \qquad (5.5)$$

where the unbracketed subscripts denote differentiation with respect to that subscript and the Jacobian coefficient $J = r_x \theta_y - r_y \theta_x = (x_r y_\theta - x_\theta y_r)^{-1}$. The major advantage of this method is that it works for any smoothly varying body surface, not just a circular cylinder. For instance, Gray & Cui (2007) used this method to compute the flow past an obliquely inclined wedge.

The system of equations (5.4) is solved numerically by a non-oscillatory central (NOC) scheme, which is a high-resolution shock-capturing method that does not require Riemann solvers. The original NOC scheme (Nessyahu & Tadmor 1990) switches between a grid, and a grid offset by half a grid cell in each direction, at alternate time steps, which can make application of the wall boundary conditions difficult. We therefore use the NOC scheme of Jiang *et al.* (1998) that uses a single grid. Figure 6(*b*) shows a typical computational domain, with a uniform distribution of circumferential grid points and a stretched radial distribution to allow a higher resolution close to the cylinder. In the experiments the radius of the cylinder $\tilde{R}$ was equal to 15 mm, which is equivalent to $R = 0.5$ dimensionless units, since the diameter $L = 30$ mm is used in the scalings (3.4). The grid covers a range from $r = 0.5$ to $r = 10$ units, with $r = 0$ at the centre of the cylinder and $(r, \theta) = (10, \pi)$ corresponding to the position of the inflow gate. The simulations can either be performed on a half grid, $0 \leqslant \theta \leqslant \pi$, with a symmetry condition along $y = 0$ or on a full grid, $0 \leqslant \theta \leqslant 2\pi$, with a wrapping condition along the grid lines $j = 1$ and $j = n_j$. Both methods have been tested and give the same results up to numerical accuracy. The results from the full-grid simulations are presented for ease of comparison with the experiments.

Initially the chute is assumed to be grain free, i.e.

$$h \equiv 0 \quad \text{at } t = 0. \qquad (5.6)$$

The gate then opens instantaneously, so that the supercritical inflow condition is

$$h = h_0, \quad \bar{u} = \bar{u}_0, \quad v = 0 \quad \text{at } x = 0, \quad t > 0, \qquad (5.7)$$

where h_0 is determined by the gate height and $\bar{u}_0$ is measured by PIV. In order to apply the inflow condition (5.7) on the O-type grid, a one-dimensional solution without an obstacle is precomputed on a rectangular grid to determine the upstream values of $h(x, t)$ and $\bar{u}(x, t)$ as the avalanche enters through the outermost upstream grid cells, i.e. $j \in [n_{j1}, n_{j3}]$ on $i = n_i$ in figure 6. The fact that the flow front remained one-dimensional, in regions that were not influenced by the cylinder, as the front propagated through the domain provided a strong test of the method. For the experiments and computations presented in this paper the downstream outflow is also supercritical, so no physical boundary conditions need to be applied for $j \in [1, n_{j1}] \cup [n_{j3}, n_j]$ on $i = n_i$. On the cylinder wall ($i = 1$) a no normal flux condition is applied

$$h\boldsymbol{u} \cdot \boldsymbol{n} = 0 \quad \text{at } r = 0.5. \qquad (5.8)$$

This condition is satisfied when either: (i) the flow is parallel to the wall, $\boldsymbol{u} \cdot \boldsymbol{n} = 0$; or (ii) the flow thickness is zero, $h = 0$. The later condition allows the grain-free vacuum boundary to detach from the wall. A cutoff threshold of $h = 10^{-3}$ non-dimensional units is used to prevent division by zero when the momentum transport terms (5.2) are computed. Following Gray *et al.* (2003) the results are plotted with the lowest contour at $h = 10^{-2}$ non-dimensional units or 300 μm, which is approximately equal

to the average diameter of a grain of sand. This mirrors the finite grain size in the experiments and prevents spurious zero thickness contour lines being depicted in the grain-free regions.

6. Time-dependent evolution of the avalanche

A series of photographs of the avalanche impinging on the circular cylinder on a slope inclined at $\zeta = 36°$ are shown in (a,c,e,g) of figures 7 and 8. A supplementary movie of the experiment is available at http://dx.doi.org/10.1017/jfm.2013.42. The pictures were taken with a shutter speed of $1/20$ of a second, a frame rate of 25 frames per second and show how the bow shock and the granular vacuum are formed in a close-up region near the cylinder (18.6 cm × 13.8 cm). The right-hand side panels (b,d,f,h) in figures 7 and 8 show contours of the evolving avalanche thickness from a corresponding numerical simulation. The time intervals between frames are equal to 0.72 non-dimensional units. The initial conditions $h_0 = 0.4$ and $\bar{u}_0 = 0.8$ and the basal angle of friction $\delta = 26°$ for the simulation were determined by the method described in § 4. The computations were performed on an O-grid with 501×251 grid points in the circumferential and radial directions, respectively.

The position of the evolving vacuum boundary, which separates the avalanching grains from grain-free region, provides a very sensitive test of the numerical simulations as its position is strongly influenced by the local velocity field, pressure gradients and source terms. The position of the boundary is superimposed on the experimental images to provide a quantitative comparison between the experiments and the simulations. Figure 7(a,b) show the avalanche front just upstream of the cylinder prior to impingement. In the experiments the front is diffuse, this is partly due to motion blur, and partly because as the depth of the flow reaches that of a single grain, the particles can start to bounce down the slope rather than avalanching *en masse*. In the numerical computations neither of these effects occur and there is a sharp front that is still uniform in the cross-slope direction. Since the gate release was out of camera shot, the simulation and the experiment were synchronized by using the front position of approximately $x = 8$ units at time $t = 7.4$ units.

As the avalanche first impinges on the obstacle (figure 7c,d) it is quite thin and travelling very fast. As a result only those particles that collide with the cylinder wall are significantly affected by the obstacle, and away from this region the flow front continues to propagate uniformly downstream. By $t = 8.84$ units the bow shock in front of the cylinder is already quite well developed (figure 7e,f) and the uniform part of the avalanche front has propagated out of camera shot. The granular vacuum lies immediately downstream of the cylinder and still has almost straight sides in the experiment, which are now much sharper and well-defined than the initial diffuse front. The computed position of this moving boundary agrees extremely well with the experiments. The bow shock continues to strengthen (figure 7g,h) growing slightly in height and moving only slightly upstream until the oblique shocks on either side of the obstacle are almost fully developed by $t = 10.28$ in figure 8(a,b). In contrast the vacuum boundary takes longer to develop. It slowly closes (figures 7g,h and 8a,b) in response to the lithostatic pressure within the body that pushes the grains sideways, before it finally pinches off just before $t = 11$ in figure 8(c,d). The pinch-off point then propagates upstream until it reaches an almost steady configuration by $t = 12.44$ in figure 8(g,h). The grain-free vacuum region therefore forms a triangular shape on the lee side of the cylinder. At all stages of the computation the spatially, temporally and topologically evolving vacuum boundary agrees extremely well with what is observed
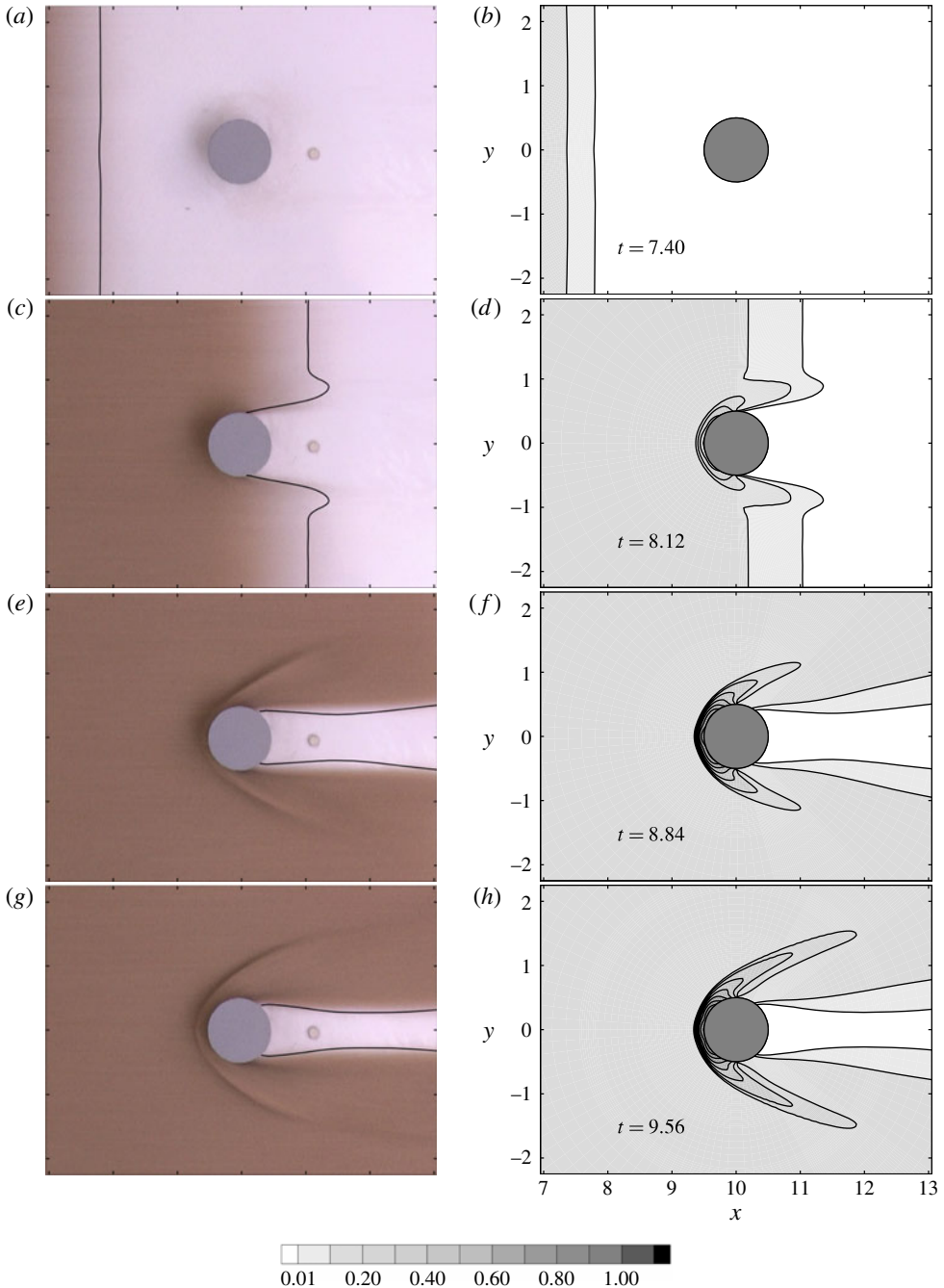
FIGURE 7. (*a,c,e,g*) Photographs and superimposed computed boundary showing the time-dependent development of a bow shock and a vacuum boundary as a sand avalanche flows around a circular cylinder on a chute inclined at $\zeta = 36°$. Consecutive images are 0.04 s apart. (*b,d,f,h*) Numerical solutions for the avalanche thickness h at corresponding times. The simulations are performed with $h_0 = 0.4$, $\bar{u}_0 = 0.8$, $\delta = 26°$ and all units are dimensionless.
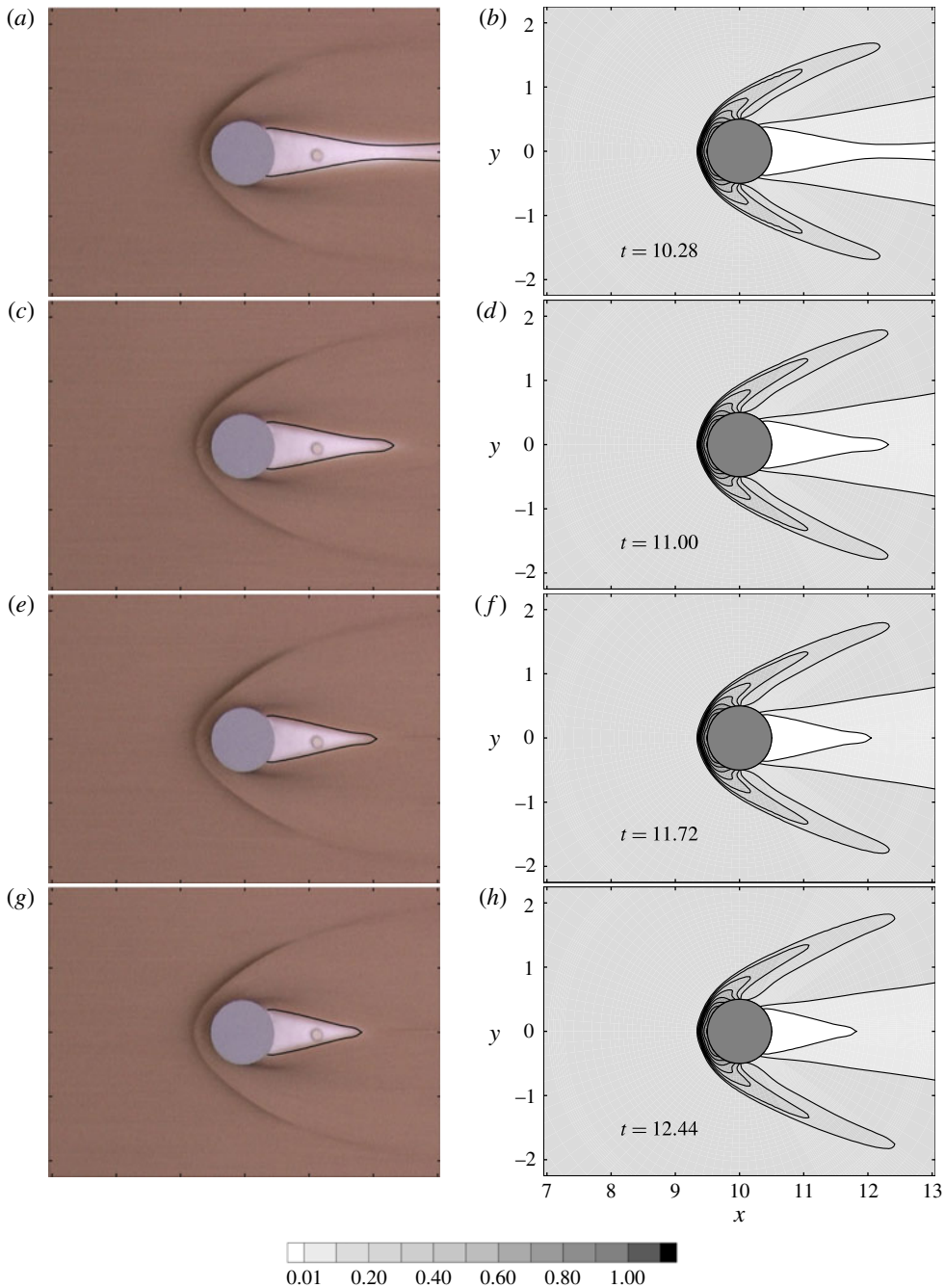
FIGURE 8. (*a,c,e,g*) Photographs and superimposed computed boundary and (*b,d,f,h*) numerical solutions showing the continuation of the time-dependent development of a bow shock and a vacuum boundary shown in figure 7. Consecutive images are 0.04 s apart, which corresponds to 0.72 non-dimensional units. A movie showing the time-dependent evolution of the experiment is available at http://dx.doi.org/10.1017/jfm.2013.42.
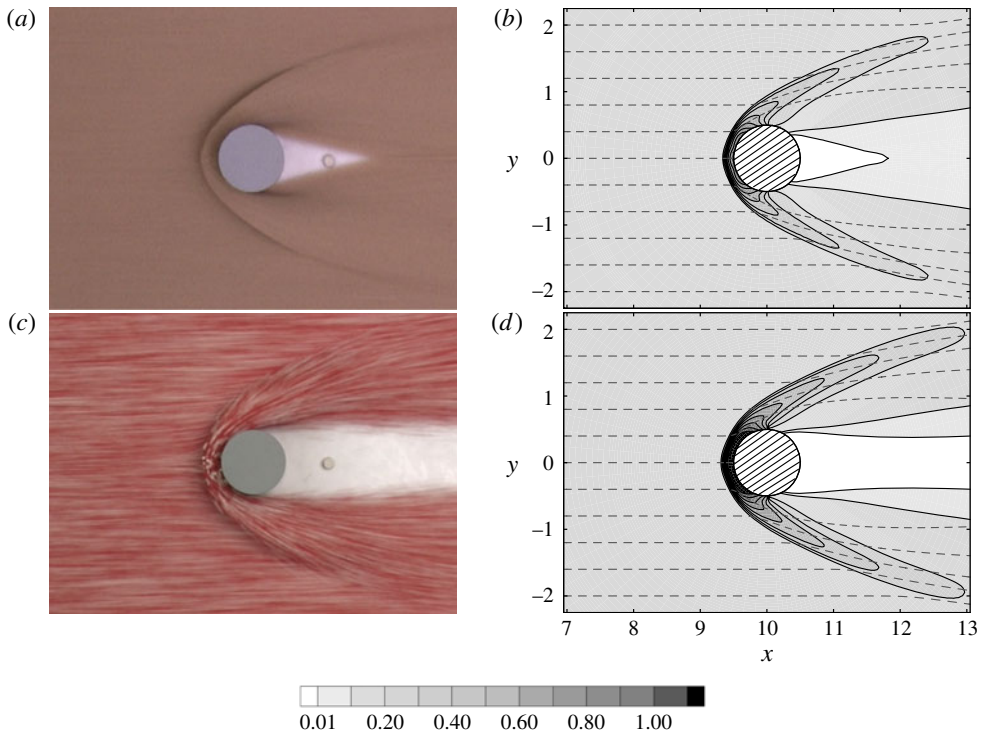
FIGURE 9. Photographs of steady-state avalanches of sand (*a*) and non-pareille grains (*c*) past a circular cylinder. The equivalent steady-state computational contours of the avalanche thickness *h* are shown in (*b,d*), respectively, together with particle paths (dashed lines). The parameters for the simulations are given in figure 5 and movies showing the time-dependent evolution of both experiments are available at http://dx.doi.org/10.1017/jfm.2013.42.

in experiments, indicating that this simple two-parameter model captures all of the essential physics.

7. Steady-state solution

At later times the experimental flow reaches a steady-state regime with no further evolution within the field of view, apart from some small fluctuations due to the slightly unsteady nature of the hopper flow. The time to reach steady state (in the field of view) after the initial impingement on the cylinder (i.e. between figures 7*a* and 8*g*) is approximately five non-dimensional time units or 0.277 s. The vacuum pinch-off occurs at a distance $x = 11.8$ in the final steady state for the sand avalanche, shown in figure 9(*a,b*), which is very slightly shorter than at $t = 12.44$. For comparison, the steady state experiment and numerical simulation for non-pareille on a slope of $\zeta = 38°$ is shown in figure 9(*c,d*). The parameters for the simulation are given in figure 5 and a movie of the experiment is available at http://dx.doi.org/10.1017/jfm.2013.42. This is particularly revealing, as one can clearly see the particles upwelling between the bow shock and the stagnation point and then being accelerated strongly in the cross-slope direction on either side of the symmetry line. The bow shock wave in the non-pareille is very similar to that in sand, but the shape and extent of
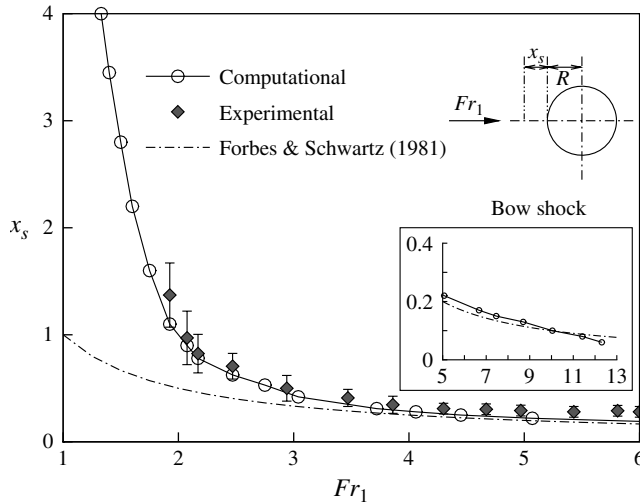
FIGURE 10. The non-dimensional detachment, or standoff, distance x_s of the bow shock as a function of the incoming Froude number Fr_1 obtained in computation (solid-line with open circles), experiment (filled diamonds) and the approximate series solution, $1/Fr_1$, of Forbes & Schwartz (1981) (dot-dash line). The upper schematic diagram shows x_s and the cylinder radius $R = 0.5$, the lower inset shows the computed and series approximation for the standoff distance for Froude numbers 5 to 13.

the granular vacuum is markedly different. These similarities and differences will be investigated below.

7.1. *Standoff distance of the bow shock*

The upstream Froude number, Fr_1, is an important parameter in the theory, which increases strongly with downstream distance due to the net acceleration of the slope. The Froude number at the inflow is approximately $Fr_0 = 2.1$ for sand and $Fr_0 = 1.4$ for non-pareille grains, but by $x = 9$, just upstream of the shock, the one-dimensional solution and parameters derived in §4 imply that $Fr_1 = 6.04$ (sand) and $Fr_1 = 6.87$ (non-pareille), respectively. Both of these are high and equivalent problems in gas dynamics would be classed as hypersonic flows (e.g. Hayes & Probstein 1966). The jump conditions for the system of avalanche equations (3.1)–(3.3) are independent of the source terms (see e.g Gray & Cui 2007), which implies that the jumps in h and $\bar{u}$ across the shocks are not directly influenced by the acceleration, although they are influenced indirectly by the changing local value of the Froude number. As the Froude numbers of the sand and the non-pareille grains are comparable at $x = 9$ the size and shape of the bow shocks are also comparable. The slightly higher value of Fr_1 for non-pareille grains produces a larger jump in height across the shock, but the standoff distance x_s of the bow shock in front of the cylinder is almost the same as that for sand.

Figure 10 shows a graph of the standoff distance, x_s, as a function of the upstream Froude number, Fr_1. The experimental values are determined by performing experiments at different slope angles and gate heights and measuring the velocity, $\bar{u}_1$, just upstream of the shock with PIV and reading off the flow height h_1 through the transparent sidewall. For $Fr_1 > 2$, the bow shock forms and has a sharp jump in thickness. The experiments show that the standoff distance decreases with increasing

Froude number, Fr_1, becoming equal to approximately one quarter of the cylinder diameter by Froude number six. For upstream Froude numbers below about two, the shocks are so diffuse that the standoff distance cannot be accurately defined. This is consistent with previous observations (Gray & Cui 2007; Johnson & Gray 2011) and suggests that the effects of the depth-averaged rheology (e.g. Forterre 2006) are sufficiently strong to prevent wave steepening.

There have been a large number of studies that have developed approximate solutions or practical empirical relations for the shock standoff distance in gas dynamics and hypersonics (e.g. Lin & Rubinov 1948; Hida 1953; Kim 1956; Lighthill 1957; Lobb 1964; Hayes & Probstein 1966; Louie & Ockendon 1991; Belouaggadia, Olivier & Brun 2008). However, despite the isomorphism between smooth shallow-water and isentropic gas dynamic flows when the ratio of specific heats $\gamma = 2$ (Preiswerk 1938; Courant & Hilbert 1962) these relations cannot be used for granular avalanches, because energy is not conserved across shocks. There are comparatively few studies for shallow-water flows. Forbes & Schwartz (1981) considered the supercritical shallow water flow past a blunt body, such as a bridge pier, that supports a detached bow shock. The problem is formulated inversely, by prescribing the upstream Froude number and the shock to be a conic section, and then calculating the location of the body by using Padé approximants to analytically continue Taylor series expansions. For a parabolic shock, Forbes & Schwartz (1981) showed that for large Fr_1, the standoff distance, x_s, is approximately equal to the reciprocal of the upstream Froude number

$$x_s \sim \frac{1}{Fr_1} \quad \text{as } Fr_1 \longrightarrow \infty. \tag{7.1}$$

This is shown by the dot-dash line in figure 10 and provides a reasonable approximation to the experimental data even at low Froude numbers. Numerical computations for the standoff distance at higher Froude numbers (figure 10 inset) also show good agreement with Forbes & Schwartz's (1981) approximation (7.1), although it becomes increasingly difficult to calculate solutions, because the magnitude of the jumps increase at the same time as the shock detachment distance becomes closer to the wall. The results suggest that at Froude number six the standoff distance should be one sixth, but measured values are closer to one quarter. There are two possible explanations for this disagreement. One possibility is that we have overestimated the experimental Froude number, Fr_1, from the PIV measurements by assuming that the flow is plug-like. An alternative possibility is that new physics comes into play, as in shallow-water flows (Mignot & Riviere 2010), where horseshoe vortices form. In the case of granular flows, a small deposit is left upstream of the cylinder when the flow ceases. The deposit looks similar to that observed by Gray *et al.* (2003) on the upstream facing side of a pyramid, but in contrast there is no evidence of it from free-surface observations during the flow. There may, however, be a subsurface static, or very slowly moving, zone adjacent to the cylinder, which would effectively change its shape, and tend to move the standoff distance further upstream.

The source terms do not significantly affect the position of the bow shock or the thickness at the stagnation point. To see this we consider the motion along the central streamline from the bow shock to the stagnation point. The mass and momentum jump conditions (see e.g. Gray & Cui 2007) across a normal shock imply that

$$h_1 \bar{u}_1 = h_2 \bar{u}_2, \tag{7.2}$$

$$h_1 \bar{u}_1^2 + \tfrac{1}{2} h_1^2 \cos \zeta = h_2 \bar{u}_2^2 + \tfrac{1}{2} h_2^2 \cos \zeta, \tag{7.3}$$

where the subscripts '1' and '2' indicate the value on the rearward and forward side of the shock, respectively. Using (7.3) to eliminate $\bar{u}_2$ in (7.3) implies that the ratio of thicknesses across the shock satisfies

$$\frac{h_2}{h_1} = \frac{\sqrt{1 + 8Fr_1^2} - 1}{2}. \tag{7.4}$$

For a steady flow with shape factor $\lambda = 1$ the downstream momentum balance equation (3.2) can be reduced to the one-dimensional steady-state equation (4.6), irrespective of the fact that both $\partial \bar{u}/\partial y \neq 0$ and $\partial \bar{v}/\partial y \neq 0$. This is because the mass balance equation (3.1) can be used to simplify the momentum transport terms and the cross-slope velocity $\bar{v}$ is equal to zero on the central streamline. Equation (4.6) can then be integrated from the shock to the stagnation point, where the downstream velocity $\bar{u}_{stag}$ is by definition zero, and the corresponding stagnation thickness is

$$h_{stag} = x_s \cos\zeta (\tan\zeta - \tan\delta) + h_2 + \frac{\bar{u}_2^2}{2\cos\zeta}. \tag{7.5}$$

For typical chute parameters and standoff distances, the first term on the right-hand side is approximately 0.04 units, which is much smaller than typical stagnation point heights, which are order unity, so the source terms play a negligible role. Substituting (4.3) and using (7.3) and (7.4) to eliminate h_2 and $\bar{u}_2$, allows the ratio of the stagnation depth to the inflow depth to be expressed in terms of the upstream Froude number

$$\frac{h_{stag}}{h_1} = \frac{x_s}{h_1} \sec\delta \sin\beta + 1 + \frac{1}{2}Fr_1^2 - \frac{1}{16}\frac{([1 + 8Fr_1^2]^{1/2} - 3)^3}{([1 + 8Fr_1^2]^{1/2} - 1)}, \tag{7.6}$$

which is the generalization of Forbes & Schwartz's (1981) result. The additional contribution from the source terms is usually very small because both $\sin\beta$ and the standoff distance x_s are small. To emphasize this point, the standoff distance for the numerical computations in figure 10 are calculated by assuming that $\mathbf{S} = \mathbf{0}$. This shows that the source terms play a negligible role for the position of the bow shock, but they do play an important role when they act over longer distances. Given the upstream flow thickness h_1 and Froude number Fr_1, (7.6) places a constraint on the minimum height of the obstacle to prevent overtopping by an avalanche. This therefore provides a very useful engineering approximation that can be used for the design of avalanche protection structures.

7.2. *Pinch-off distance of the granular vacuum*

Since the Froude numbers just upstream of the cylinder are comparable in the steady-state experiments shown in figure 9(a,c), the major difference between them is the acceleration that the grains experience. The parameter $\beta = \zeta - \delta$ introduced in (4.4) is useful, as it determines the net acceleration of an avalanche down an incline. Slopes are described as being accelerative if $\beta > 0$, non-accelerative if $\beta = 0$ and decelerative if $\beta < 0$. For typical basal angles of friction, $\sec\delta$ is just above unity and therefore the term $\sin\beta$ in the source term (4.3) controls the effective acceleration in the downslope momentum balance equation (4.2). The slopes in figure 9 are both accelerative, with $\beta = 10°$ for sand and $\beta = 15°$ for non-pareille grains. While a five-degree difference in β may not seem much, it represents a 50 % increase, and it is sufficient to significantly affect the position and shape of the vacuum boundary. Indeed the non-pareille vacuum boundary is still almost the same width as the cylinder at the edge of the photograph
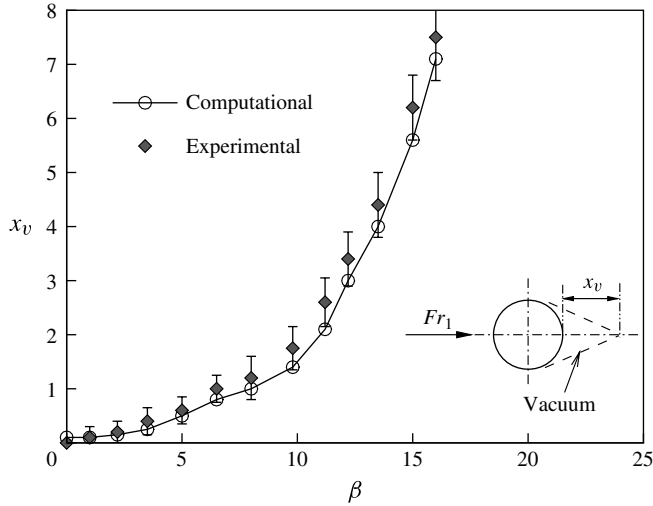
FIGURE 11. The non-dimensional vacuum pinch-off distance x_v for fixed inflow height $h_0 = 0.43$ as a function of the net acceleration angle $\beta = \zeta - \delta$ obtained from computation (solid line with open circles) and experiment (filled diamonds). The inset is a schematic showing x_v. Note that these experiments and computations have been performed by changing the angle ζ of the chute. This alters both the inflow Froude number and evolution of the Froude number along the chute.

in figure 9(*c*), which contrasts with the short triangular vacuum in sand (figure 9*a*). This sensitivity of the position of the vacuum boundary, therefore provides an exacting test for theoretical models.

For the non-pareille experiments the upstream Froude number ($Fr_1 = 6.87$) is higher than that for sand ($Fr_1 = 6.04$) and as the grains move around the cylinder they have more momentum. The expansion is therefore not quite as strong. As a result the vacuum boundary detaches from either side of the cylinder slightly higher upstream and the initial angle of closure is significantly less. The simple avalanche model described in §3 suggests that the vacuum will always close. This is because if the lateral velocity, $v = 0$, the cross-slope source term, S_2, defined in (3.6), is zero, and hence the lateral pressure gradients in (3.3) will apply a force that drives particles into the vacuum. Evidence for this is provided by the streak lines in figure 9(*c*). Close to the vacuum-detachment point the particle paths are initially directed outwards, but slowly bend inwards and begin to converge, although the pinch-off point lies out of shot. A numerical simulation of the avalanche using the parameters determined in §4 accurately reproduces the slow closure of the non-pareille vacuum (figure 9*d*) as well as the triangular shape for sand (figure 9*b*).

Figure 11 shows the pinch-off distance x_v, which is defined as the distance from the rear of the cylinder to the pinch-off point, as a function of the net acceleration angle β for a fixed inflow height $h_0 = 0.43$. The experimental data points were determined by varying the slope angle from $\zeta = 23$–$40°$ for the non-pareille grains (i.e. $\beta = 0$–$17°$) and measuring the pinch-off distance x_v. The initial velocity, $\bar{u}_0$, was also measured for each increment in ζ and a series of corresponding numerical simulations were performed. From figure 11 it can be seen that the pinch-off distance between the experiment (filled diamonds) and the computation (open circles line) agrees well for a broad range of the accelerating angle β. When β tends to zero,

the pinch-off distance approaches zero too, indicating that the granular vacuum closes up almost immediately behind the cylinder. For larger values of β the extent of the vacuum increases nonlinearly rising rapidly to about eight non-dimensional units at a slope angle $\zeta = 40°$. As the inclination angle is increased the average Froude number increases as well as its variation along the chute. Higher Froude numbers suggest thinner faster moving flows, where the pressure gradients play less of a role, the vacuum closes more slowly and the pinch-off distance therefore extends further downstream.

7.3. *Wake development*

Heil *et al.* (2004) investigated the 'V'-shaped Mach cone that developed as a thin cylindrical rod was moved rapidly horizontally through a thin layer of vibro-fluidized granular material. They drew a parallel with gas dynamics and shallow water theory and experimentally verified that the half-angle of the Mach cone θ satisfied the classical relation $\sin\theta = c/u_{rod}$, where $c = \sqrt{gh}$. They also identified a scaling law (Landau & Lifshitz 1959) for the decay of the shock height $\tilde{h}_{max}$ with increasing cross-slope distance y, which should be $\tilde{h}_{max} \propto y^{-3/2}$. Heil *et al.* (2004) showed that their experiments were in good agreement with this scaling in the range $\tilde{y}/D = 3$ and 15. We have been unable to test this hypothesis against our simulations, because our grid is simply not big enough, but we anticipate deviations away from this relation, because our flow continues to be accelerated with increasing downstream distance.

8. Discussion and conclusions

Small-scale experiments with sand and non-pareille grains have been used to show that when a granular avalanche flows around a circular cylinder, a bow shock wave is generated in front of it, and on the lee side there is a grain-free granular vacuum. Numerical simulations are used to show that a simple two-parameter depth-averaged avalanche model (e.g. Gray *et al.* 2003) is able to accurately predict the position of the bow shock and the granular vacuum. The simulations rely on a boundary fitted coordinate system (Vinokur 1974; Viviand 1974) and the use of a high-resolution shock-capturing numerical method (Nessyahu & Tadmor 1990; Jiang *et al.* 1998). It is sufficiently general to be able to calculate the flow around any smooth walled obstacle (with the wall normal to the slope). In order to prescribe the upstream boundary conditions correctly, it is necessary to calculate a one-dimensional solution for the undisturbed flow, as it enters the body-fitted mesh. The results for the temporal and spatial development of the bow shock and the vacuum boundary are in very good agreement with the experiments (see figures 7 and 8). Indeed even the slow upstream propagation of the vacuum pinch-off point (figure 8) before steady state is reached, is reproduced accurately by the scheme. Experimentally the shock standoff distance is seen to decrease with increasing upstream Froude number, reaching approximately a quarter of the cylinder diameter at Froude number six (figure 10). Our numerical simulations and previous approximate solutions (Forbes & Schwartz 1981) imply that as the Froude number tends to infinity the standoff distance continues to reduce as the reciprocal of the Froude number (7.1). This leads to a small discrepancy with the experimental data near $Fr_1 = 6$, which might be due to the formation of a subsurface dead zone. The position of the bow shock is not strongly influenced by the source terms, but the closure rate of the vacuum is very sensitive to the net acceleration $\beta = \zeta - \delta$. As the difference between the slope inclination angle ζ and the

dynamic basal angle of friction δ increases, the pinch-off point moves far downstream (figure 11).

These results are of practical importance for natural hazards, such as snow avalanches, rockfalls, debris flows, lahars and pyroclastic flows, which frequently impinge on obstacles such as trees (Cole *et al.* 1998; Gray & Kokelaar 2010) or pylons (Hauksson *et al.* 2007; Sovilla *et al.* 2008; Hu, Wei & Li 2011). For engineers a fundamental task is to determine the impact pressures and dynamic loadings that man-made structures need to be able to withstand, as well as the necessary height of the obstacles to prevent overtopping by an avalanche. The shape of the obstacle and the angle that the avalanche impinges upon it have an important effect on whether shock waves will detach to form bow waves or not (Cui *et al.* 2007; Gray & Cui 2007; Baroudi, Sovilla & Thibert 2011). However, when detached shocks do form, the simple relation (7.6) for the ratio of the stagnation height to the inflow height at a given Froude number, may provide a useful engineering approximation for optimizing the height of the obstacle.

At the European avalanche test site at the Vallée de la Sionne in Switzerland an instrumented mast is used to make measurements of the flow velocity in the dense basal avalanche. The measurements are made by cross-correlation of optical sensors that are placed on an obliquely inclined wedge. Understanding the flow around such masts is of crucial importance in interpreting the resulting data. For instance, if an oblique shock wave is generated by the wedge, then the undisturbed upstream conditions can be inferred by using the oblique shock relations (e.g. Gray *et al.* 2003; Hákonardóttir & Hogg 2005; Cui *et al.* 2007; Gray & Cui 2007; Jóhannesson *et al.* 2009). This has not yet been done at the Vallée de la Sionne, although measured velocities seem consistent with order of magnitude estimates of the avalanche flow speed, and are probably at most 20 % smaller than the undisturbed upstream values. The flow thickness at the mast is measured by the depression of switches, and can be significantly thicker than the upstream flow, suggesting that inferred downstream Froude numbers ($1 \leqslant Fr_2 < 6$) may be considerably less than the real upstream values. The mast also has a number of blunt surfaces, which suggest that it is possible for a bow shock to form. If this is the case then it becomes almost impossible to relate downstream velocity data to the upstream conditions, because the flow velocity varies from zero near the stagnation point to quite large values over a very short distance. There is therefore still scope to optimize the design of instrumented masts in order to reliably relate upstream flow conditions to measurements made adjacent to the obstacle wall, i.e. to eliminate all possibility of shock detachment. Conversely, in order to optimize the design of avalanche protection structures, not used for velocity measurement, it may be beneficial to promote the formation of detached bow shocks, because much more energy is dissipated in strong shocks than in weak shocks (Gray & Cui 2007).

Supplementary movies

Supplementary movies are available at http://dx.doi.org/10.1017/jfm.2013.42.

REFERENCES

AKERS, B. & BOKHOVE, O. 2008 Hydraulic flow through a channel contraction: multiple steady states. *Phys. Fluids* **20**, 056601.

AMES RESEARCH STAFF, 1953 Equations, tables and charts for compressible flow. *Tech. Rep.* 1135. NACA.

ANDERSON, J. D. 1995 *Computational Fluid Dynamics*. McGraw-Hill.

BAROUDI, D., SOVILLA, B. & THIBERT, E. 2011 Effects of flow regime and sensor geometry on snow avalanche impact-pressure measurements. *J. Glaciol.* **57**, 277–288.

BELOUAGGADIA, N., OLIVIER, H. & BRUN, R. 2008 Numerical and theoretical study of the shock stand-off distance in non-equilibrium flows. *J. Fluid Mech.* **607**, 167–197.

BÖRZSÖNYI, T., HALSEY, T. C. & ECKE, E. 2008 Avalanche dynamics on a rough inclined bed. *Phys. Rev.* E **78**, 011306.

BOUDET, J. F., AMAROUCHENE, Y., BONNIER, B. & KELLAY, H. 2007 The granular jump. *J. Fluid Mech.* **572**, 413–431.

BOUDET, J. F. & KELLAY, H. 2010 Drag coefficient for a circular obstacle in a quasi-two-dimensional dilute supersonic granular flow. *Phys. Rev. Lett.* **105**, 104501.

BRANNEY, M. J. & KOKELAAR, B. P. 1992 A reappraisal of ignimbrite emplacement: progressive aggradation and changes from particulate to non-particulate flow during emplacement of high-grade ignimbrite. *Bull. Volcanol.* **54**, 504–520.

BRENNEN, C. E., SIECK, K. & PASLASKI, J. 1983 Hydraulic jumps in granular material flow. *Powder Technol.* **35**, 31–37.

BUCHHOLTZ, V. & PÖSCHEL, T. 1998 Interaction of a granular stream with an obstacle. *Granul. Matt.* **1**, 33–41.

COLE, P. D., CALDER, E. S., DRUITT, T. H., HOBLITT, R., ROBERTSON, R., SPARKS, R. S. J. & YOUNG, S. R. 1998 Pyroclastic flows generated by gravitational instability of the 1996–97 lava dome of Soufriere Hills Volcano, Montserrat. *Geophys. Res. Lett.* **25**.

COURANT, R. & FRIEDRICHS, K. O. 1948 *Supersonic Flow and Shock Waves*. Interscience.

COURANT, R. & HILBERT, D. 1962 *Methods of Mathematical Physics*, vol. II. Interscience.

CUI, X., GRAY, J. M. N. T. & JOHANNESSON, T. 2007 Deflecting dams and the formation of oblique shocks in snow avalanches at Flateyri, Iceland. *J. Geophys. Res.* **112**, F04012.

FAUG, T., GAUER, P., LIED, K. & NAAIM, M. 2008 Overrun length of avalanches overtopping catching dams: cross-comparison of small-scale laboratory experiments and observations from full-scale avalanches. *J. Geophys. Res.* **113**, F03009.

FORBES, L. K. & SCHWARTZ, L. W. 1981 Supercritical flow past blunt bodies in shallow water. *Z. Angew. Math. Phys.* **32**, 314–328.

FORTERRE, Y. 2006 Kapiza waves as a test for three-dimensional granular flow rheology. *J. Fluid Mech.* **563**, 123–132.

GODUNOV, S. K. 1959 A difference scheme for numerical solution of discontinuous solution of hydrodynamic equations. *Math. Sbornik.* **47**, 271–306.

GRAY, J. M. N. T. 2001 Granular flow in partially filled slowly rotating drums. *J. Fluid Mech.* **441**, 1–29.

GRAY, J. M. N. T. & CUI, X. 2007 Weak, strong and detached oblique shocks in gravity driven granular free-surface flows. *J. Fluid Mech.* **579**, 113–136.

GRAY, J. M. N. T. & HUTTER, K. 1997 Pattern formation in granular avalanches. *Contin. Mech. Thermodyn.* **9**, 341–345.

GRAY, J. M. N. T. & KOKELAAR, B. P. 2010 Large particle segregation, transport and accumulation in granular free-surface flows. *J. Fluid Mech.* **652**, 105–137.

GRAY, J. M. N. T. & TAI, Y. C. 1998 Particle size segregation, granular shocks and stratification patterns. In *Physics of Dry Granular Media* (ed. H. J. Herrmann, J. P. Hovi & S. Luding). NATO ASI Series, vol. 350, pp. 697–702.

GRAY, J. M. N. T., TAI, Y. C. & NOELLE, S. 2003 Shock waves, dead-zones and particle-free regions in rapid granular free-surface flows. *J. Fluid Mech.* **491**, 161–181.

GRAY, J. M. N. T., WIELAND, M. & HUTTER, K. 1999 Free surface flow of cohesionless granular avalanches over complex basal topography. *Proc. R. Soc.* A **455**, 1841–1874.

GRIGOURIAN, S. S., EGLIT, M. E. & IAKIMOV, I. L. 1967 New statement and solution of the problem of the motion of snow avalanche. *Snow, Avalanches & Glaciers. Tr. Vysokogornogo Geofizich. Inst.* **12**, 104–113.

HÁKONARDÓTTIR, K. M. & HOGG, A. J. 2005 Oblique shocks in rapid granular flows. *Phys. Fluids* **17**, 0077101.

HÁKONARDÓTTIR, K. M., HOGG, A. J., BATEY, J. & WOODS, A. W. 2003 Flying avalanches. *Geophys. Res. Lett.* **30**, 2191.

HAUKSSON, S., PAGLIARDI, M., BARBOLINI, M. & JÓHANNESSON, T. 2007 Laboratory measurements of impact forces of supercritical granular flow against mast-like obstacles. *Cold Reg. Sci. Technol.* **49**, 54–63.

HAYES, W. D. & PROBSTEIN, R. F. 1966 *Hypersonic Flow Theory*. Academic.

HEIL, P., RERICHA, E. C., GOLDMAN, D. I. & SWINNEY, H. L. 2004 Mach cone in a shallow granular fluid. *Phys. Rev.* E **70**, 060301.

HIDA, K. 1953 An approximate study of the detached shock wave in front of a circular cylinder and a sphere. *J. Phys. Soc. Japan* **8**, 740–745.

HU, K., WEI, F. & LI, Y. 2011 Real-time measurement and preliminary analysis of debris-flow impact force at Jiangjia Ravine, China. *Earth Surf. Process. Landf.* **36**, 1268–1278.

HUNGR, O. & MORGENSTERN, N. R. 1984a Experiments on the flow behaviour of granular materials at high velocity in an open channel flow. *Geotechnique* **34**, 405–413.

HUNGR, O. & MORGENSTERN, N. R. 1984b High velocity ring shear tests on sand. *Geotechnique* **34**, 415–421.

IPPEN, A. T. 1949 Mechanics of supercritical flow. *ASCE* **116**, 268–295.

IVERSON, R. M. 1997 The physics of debris-flows. *Rev. Geophys.* **35**, 245–296.

IVERSON, R. M. & DENLINGER, R. P. 2001 Flow of variably fluidized granular masses across three-dimensional terrain 1. Coulomb mixture theory. *J. Geophys. Res.* **106** (B1), 553–566.

JIANG, G. S., LEVY, D., LIN, C. T., OSHER, S. & TADMOR, E. 1998 High-resolution nonoscillatory central schemes with non-staggerred grids for hyperbolic conservation laws. *SIAM J. Numer. Anal.* **35** (6), 2147–2168.

JÓHANNESSON, T. 2001 Run-up of two avalanches on the deflecting dams at Flateyri, northwest Iceland. *Ann. Glaciol.* **32**, 350–354.

JÓHANNESSON, T., GAUER, P., ISSLER, P. & LIED, K. 2009 The design of avalanche protection dams: recent practical and theoretical developments. *Tech. Rep.* EUR 23339. European Commission.

JOHNSON, C. G. & GRAY, J. M. N. T. 2011 Granular jets and hydraulic jumps on an inclined plane. *J. Fluid Mech.* **675**, 87–116.

JOHNSON, C. G., KOKELAAR, B. P., IVERSON, R. M., LOGAN, M., LAHUSEN, R. G. & GRAY, J. M. N. T. 2012 Grain-size segregation and levee formation in geophysical mass flows. *J. Geophys. Res.* **117**, F01032.

JOMELLI, V. & BERTRAN, P. 2001 Wet snow avalanche deposits in the French Alps: structure and sedimentology. *Geografis. Annal. Ser.* A, *Phys. Geograph.* **83**, 15–28.

KIM, C. S. 1956 Experimental studies of supersonic flow past a circular cylinder. *J. Phys. Soc. Japan* **11**, 439–445.

LANDAU, L. D. & LIFSHITZ, E. M. 1959 *Fluid Mechanics*. Pergamon.

LEVEQUE, R. J. 2002 *Finite Volume Methods for Hyperbolic Problems*. Cambridge University Press.

LIGHTHILL, M. J. 1957 Dynamics of a dissociating gas. part 1. equilibrium flow. *J. Fluid Mech.* **2**, 1–32.

LIN, C. C. & RUBINOV, S. I. 1948 On the flow behind curved shocks. *J. Math. Phys.* **27**, 105–129.

LOBB, R. K. 1964 Experimental measurement of shock detachment distance on spheres fired in air at hypervelocities. In *The High Temperature Aspects of Hypersonic Flow* (ed. W. C. Nelson), pp. 519–527. Pergamon.

LOUIE, K. & OCKENDON, J. R. 1991 Mathematical aspects of the theory of inviscid hypersonic flow. *Phil. Trans. R. Soc.* A **335**, 121–138.

MANGENEY, A., BOUCHUT, F., THOMAS, N., VILOTTE, J. P. & BRISTEAU, M. O. 2007 Numerical modeling of self-channeling granular flows and of their levee-channel deposits. *J. Geophys. Res.* **112**, F02017.

MANGENEY-CASTELNAU, A., VILOTTE, J. P., BRISTEAU, M. O., PERTHAME, B., BOUCHUT, F., SIMEONI, C. & YERNENI, S. 2003 Numerical modeling of avalanches based on Saint-Venant equations using a kinetic scheme. *J. Geophys. Res.* **108**, 2527.

MIGNOT, E. & RIVIERE, N. 2010 Bow-wave-like hydraulic jump and horseshoe vortex around an obstacle in a supercritical open channel flow. *Phys. Fluids* **22**, 117105.

NESSYAHU, H. & TADMOR, E. 1990 Non-oscillatory central differencing for hyperbolic conservation laws. *J. Comput. Phys.* **87**, 408–463.

POULIQUEN, O. 1999 Scaling laws in granular flows down rough inclined planes. *Phys. Fluids* **11** (3), 542–548.

POULIQUEN, O. & FORTERRE, Y. 2002 Friction law for dense granular flows: application to the motion of a mass down a rough inclined plane. *J. Fluid Mech.* **453**, 133–151.

PREISWERK, E. 1938 Anwendung gasdynamischer Methoden auf Wasserströmungen mit freier Oberfläche. PhD thesis, ETH Zürich.

RERICHA, E. C., BIZON, C., SHATTUCK, M. & SWINNEY, H. 2002 Shocks in supersonic sand. *Phys. Rev. Lett.* **88**, 014302.

ROUSE, H. 1938 *Fluid Mechanics for Hydraulic Engineers*. McGraw-Hill.

SAVAGE, S. 1979 Gravity flow of cohesionless granular materials in chutes and channels. *J. Fluid Mech.* **92**, 53–96.

SAVAGE, S. B. & HUTTER, K. 1989 The motion of a finite mass of granular material down a rough incline. *J. Fluid Mech.* **199**, 177–215.

SHINBROT, T. & MUZZIO, F. J. 1998 Reverse buoyancy in shaken granular beds. *Phys. Rev. Lett.* **81** (20), 4365–4368.

SIGURDSSON, F., TOMASSON, G. G. & SANDERSEN, F. 1998 Avalanche defences for flateyri, iceland. from hazard evaluation to construction of defences. *Tech. Rep.* 203. Norw. Geotech. Inst., Oslo.

SOVILLA, B., SCHAER, M., KERN, M. & BARTELT, P. 2008 Impact pressures and flow regimes in dense snow avalanches observed at the Vallée de la Sionne test site. *J. Geophys. Res.* **114**, F01010.

TAI, Y. C., GRAY, J. M. N. T., HUTTER, K. & NOELLE, S. 2001 Flow of dense avalanches past obstructions. *Annal. Glaciol.* **32**, 281–284.

TAI, Y. C., WANG, Y. Q., GRAY, J. M. N. T. & HUTTER, K. 1999 Methods of similitude in granular avalanche flows. In *Advances In Cold-Region Thermal Engineering And Sciences: Technological, Environmental and Climatological Impact* (ed. K. Hutter, Y. Q. Wang & H. Beer), Lecture Notes in Physics, vol. 533, pp. 415–428. Springer.

VALLANCE, J. W. 2000 Lahars. In *Encyclopedia of Volcanoes* (ed. H. Sigurdsson), pp. 601–616. Academic.

VINOKUR, M. 1974 Conservation equations of gas dynamics in curvilinear coordinate systems. *J. Comput. Phys.* **14**, 105–125.

VIVIAND, H. 1974 Conservative forms of gas dynamic equations. *Rech. Aerosp.* **1971-1**, 65–68.

VREMAN, A. W., AL-TARAZI, M., KUIPERS, J. A. M., VAN SINT ANNALAND, M. & BOKHOVE, O. 2007 Supercritical shallow granular flow through a contraction: experiment, theory and simulation. *J. Fluid Mech.* **578**, 233–269.

WASSGREN, C. R., CORDOVA, J. A., ZENIT, R. & KARION, A. 2003 Dilute granular flow around an immersed cylinder. *Phys. Fluids* **15** (11), 3318–3330.

WIELAND, M., GRAY, J. M. N. T. & HUTTER, K. 1999 Channelised free surface flow of cohesionless granular avalanches in a chute with shallow lateral curvature. *J. Fluid Mech.* **392**, 73–100.